Journal of Solid State Chemistry **155,** 273–279 (2000)
doi:10.1006/jssc.2000.8793, available online at http://www.idealibrary.com on IDEAL®

The Influence of Particle Size on Sintering and Conductivity of $Bi_{0.85}Pr_{0.105}V_{0.045}O_{1.545}$ Ceramics

M. Benkaddour, M.C. Steil, M. Drache,[1] and P. Conflant

Laboratoire de Cristallochimie et Physicochimie du Solide, UPRES A 8012, ENSCL et USTL, B.P. 108, 59652 Villeneuve d'Ascq Cedex, France

Received February 29, 2000; in revised form June 1, 2000; accepted June 16, 2000; published online November 29, 2000

Physical characteristics of sintered pellets (relative density, microstructure, electrical conductivity level) of the fluorite-type mixed oxide, $Bi_{0.85}Pr_{0.105}V_{0.045}O_{1.545}$, have been investigated and correlated with the granularity of the powder. Particle size optimization, observed by laser granulometry and SEM of powder prepared by conventional syntheses, has been achieved by attrition treatment, which decreases the particle size and increases the final relative density from 84 to 98% at 900°C. Conductivity increases by a factor of 2 in the temperature range 300–800°C.

Key Words: **bismuth-based mixed oxide; bismuth-based fluorite-type oxide; sintering process; particle size; oxide conductor; attrition treatment; shrinkage material; impedance spectroscopy; electrical conductivity.**

1. INTRODUCTION

δ-Bi_2O_3, the high-temperature form stable between 730 and 825°C, is an excellent solid electrolyte with significant oxide conductivity ($\sigma \approx 1$ S.cm^{-1} at 780°C) (1). It adopts an anionic deficient fluorite-type structure (2). Numerous metal oxide–Bi_2O_3 reactions lead to substitution of other cations for Bi^{3+} and, depending upon the oxidation state of the substituting cation, to an evolution of the vacancy number. In most cases, sample quenching leads to a significant domain of the fcc metastable phase derived from the high-temperature δ-Bi_2O_3 form. Solid solutions of this type are obtained for the Bi_2O_3–(CaO, Y_2O_3, or Sm_2O_3) (3–6) binary systems, and for the Bi_2O_3–PbO–(CaO, Y_2O_3, or Sm_2O_3) (5, 7, 8) or Bi_2O_3–V_2O_5–(Y_2O_3 or Ln_2O_3) (9) (Ln = Sm, Eu, Gd, Tb, Dy, Er, Yb) ternary systems. Of the latter (9), due to the correlation observed between Bi concentration and ionic conductivity, the $Bi_{0.85}Ln_{0.15(1-x)}V_{0.15x}O_{1.5+0.15x}$ mixed oxides, found in the bismuth-rich part of the phase diagram, were of particular interest. Substitution of V for Ln increases structure stability by decreasing the oxide vacancy number, but diminishes the electrical conductivity of the ceramic. For commercial application, the balance of properties was observed for $Bi_{0.85}Ln_{0.105}V_{0.045}O_{1.545}$ ($x = 0.3$). σ is nearly independent of lanthanide identity at high temperature (> 700°C; domain of stability of the δ-phase), whereas a slight increase in isothermal σ with increasing Ln size occurs at lower temperatures (< 400°C; δ-metastable phase). The closer the Bi^{3+} and Ln^{3+} radii, the higher the conductivity. Moreover, an apparently anomalous high conductivity level is observed for Ln = Tb ($\sigma = 10^{-3}$ S.cm^{-1} at 300°C), likely due to the specific electronic structure of this element, which can exist in two stable oxidation states, Tb^{3+} and Tb^{5+}.

On the basis of this work, we have undertaken a further investigation of homologous mixed oxides containing the largest lanthanides (La, Pr, Nd), particularly Pr for which higher conductivity could be expected. The ionic radii of Pr^{3+} and Bi^{3+} are very similar (10, 11). Moreover, praseodymium can also exhibit two stable oxidation states. This work, which did not produce materials with any significant electronic conductivity and which led us to adopt the formula, $Bi_{0.85}Pr_{0.105}V_{0.045}O_{1.545}$ for the Bi^{3+}-, Pr^{3+}-, V^{5+}-, and O^{2-}-containing material, will be described elsewhere (12).

Previous research on the bismuth-based fluorite-type oxides, and on the bismuth-based oxide conductors of other structural types, has largely concentrated on issues associated with composition and/or structure plus electrical transport properties. Possible correlations between particle size of the powder samples, sintering behavior, and electrical properties (13, 14) have not been fully explored. This paper deals with the existence of such relationhips for the fluorite-type $Bi_{0.85}Pr_{0.105}V_{0.045}O_{1.545}$ mixed oxide.

2. EXPERIMENTAL PROCEDURE

2.1. Synthesis and Characterization of Raw Material in Powder Form

$Bi_{0.85}Pr_{0.105}V_{0.045}O_{1.545}$ powder has been synthesized by the solid state reaction of stoichiometric amounts of the

[1] To whom correspondence should be addressed. Fax: (33)3 20 43 68 14. E-mail: drache@ensc-lille.fr.

0022-4596/00 $35.00

following oxides: Bi_2O_3 (Riedel de Hahn, purity > 99.6%), Pr_6O_{11} (Aldrich, >99.99%), and V_2O_5 (Aldrich, >99.99%). Bi_2O_3 and Pr_6O_{11} (commercial products) were heated for several hours at 600 and 700°C, respectively, to eliminate any traces of carbonates or hydrates. The mixture of starting materials (approximately 80 g) was dispersed in ethanol and milled, using alumina milling media, for 1 h in a centrifugal ball mill (Retsch). Two treatments (15 h each) at 700 and 800°C, with intermediate grinding allowed to complete conversion of the reactants to a pure fluorite-type phase as characterized by Guinier de Wolff powder X-ray diffraction.

The $Bi_{0.85}Pr_{0.105}V_{0.045}O_{1.545}$ synthesized has been identified by its X-ray diffraction diagram as obtained on a Siemens D5000 diffractometer using Bragg Brentano geometry, with back monochromated Cu$K\alpha$ radiation. The diffraction diagram was scanned using steps of 0.02° (2θ) over the angle range 20–130°, with a counting time of 1.5 s per step. The sample was rotated at 3.14 rad s^{-1} in order to minimize orientation effects resulting from material compactness. The positions of the peaks were determined by means of the software package DIFFRACT-AT from SOCABIM. Reflections were indexed on the basis of a fcc cell, and lattice parameters were refined using a least-squares method.

A small quantity (approximately 10 g) of the sample was set aside and the remaining material was wet ground as an ethanol slurry using an ATTRITOR NETZSCH PE 075 apparatus.

Attrition conditions were as follows: milling media was zircona balls (diameter 2 mm), powder weight was 70 g, the amount of ethanol used was 130 g, and speed was at the rate of 1000r/min.

Samples of approximately 1 g each were removed after 1, 2, 3, and 4 h of grinding for granulometric analysis. Based on scanning electron microscopy (SEM, JEOL 5300 microscope) and determination of particle mean size (MALVERN laser analyzer), an attrition treatment of 4 h was considered to be sufficient. After grinding, the powder was dried for 60 h in an oven (70–80°C).

Hereafter we shall identify each sample as *nat* or *at*, respectively, corresponding to powder receiving *n*o *a*ttrition *t*reatment or alternatively receiving 4 h of *a*ttrition *t*reatment.

2.2. Densification of the Material

Prior to investigation of $Bi_{0.85}Pr_{0.105}V_{0.045}O_{1.545}$ sintering, an evaluation of the melting temperature has been carried out by differential thermal analysis using platinum crucibles. The raw material begins to melt at about 1000°C.

Pellets were fabricated from *nat*-powder and *at*-powder previously passed through a sieve of size 200 μm (diameter 5 mm; thickness ≅ 5 mm; soft uniaxial hand pressing). Non-isothermal sintering behavior was investigated using a LINSEIS L75 dilatometer with a heating rate of 4°C/min between 20 and 900°C.

For each powder sample, three pellets were prepared under similar conditions (same mass; same uniaxial pressure; diameter 10 mm; thickness 4–5 mm) and then sintered during a thermal cycle (heating–cooling rate 4°C/min with isothermal treatment at 900°C for 1 h). To obtain an accurate relative density of sintered material, the average of the experimental density/theoretical density for the three pellets prepared from each sample (*nat* and *at*) was calculated. The theoretical density of $Bi_{0.85}Pr_{0.105}V_{0.045}O_{1.545}$ (8.52 g/cm^3) was evaluated from the formula unit mass, $Z = 4$, and the cell parameters were refined from the X-ray diffraction pattern ($a = 5.5532(3)$ Å). For each sample one pellet was used for the SEM investigation, another for the conductivity investigation, and a third was retained for a possible complementary study.

The ceramic microstructure of the polished (SiC paper 500–4000) and thermally etched (850°C for 20 min) surface of the sintered pellets was examined using a JEOL JSM-5300 scanning electron microscope.

2.3. Characterisation of Conductivity

The pellets screened for conductivity were equipped with gold electrodes vacuum deposited by sputtering on opposite flat faces. The study was performed under atmospheric pressure.

Electrical measurements were performed by impedance spectroscopy using a Solartron 1260 impedance meter (frequency range 0.1–10^7 Hz at 200°C). A Solartron 1255 frequency response analyzer operational in the frequency range 1–10^6 Hz was used to measure conductivity versus temperature between 200 and 800°C, with temperature steps of 20°C. Values were recorded after 1 h of stabilization.

Analysis of measurements was accomplished using a Z view for Windows (Scribner Associates, Inc., Southern Pines, NC 28387). The semicircle parameters (diameter = resistance R (Ω); the depression angle of semicircle center β (°); and the relaxation frequency f^0 (Hz)) were determined. The values of the conductivity σ and capacitance C at $RC\omega^0 = 1$ ($\omega^0 = 2\omega f^0$), corresponding to sintered *nat* and *at* material, were then corrected, taking into account the geometry of the pellets, the electrical characteristics of the cell, and the input circuitry of the equipment used (Solartron 1255 or 1260).

3. RESULTS AND DISCUSSION

3.1. Characteristics of the Powder

Homologous with $Bi_{0.85}Ln_{0.105}V_{0.045}O_{1.545}$ (Ln = Sm–Dy, Er, Yb, and Y), the mixed oxide, $Bi_{0.85}Pr_{0.105}V_{0.045}O_{1.545}$, adopts an anionic deficient fluorite-type structure (8). Its

X-ray diffraction pattern, typical of a fcc cell, is presented in Fig. 1. Table 1 lists calculated and observed d spacings and relative intensities of the reflections indexed according to lattice constant $a = 5.5532(3)$ Å, and refined using a least-squares method.

Figure 2 shows the evolution, versus milling time, of mean particle size, determined using a laser grain-size meter: 50 vol% of the powder was less than d_{50}. This mean size decreases drastically from 7.3 down to 0.4 μm after 2 h of attrition treatment and then does not vary significantly. Figures 3a and 3b display the statistical distributions (%) versus the particle size for *nat*-powder and *at*-powder (4 h attrition), respectively; ◆ indicates the percentage of grains for the considered size whereas ▲ corresponds to the percentage of volume occupied by the grains with a size ≤ considered size. The *nat*-powder shows a bimodal particle size distribution with a primary maximum at 11 μm and a secondary maximum at 0.3 μm; the *at*-powder has a narrow and mono-modal particle size distribution. The attrition treatment applied to raw material, which has a particle size distribution centered at 11 μm, rapidly diminishes the mean size of the particles.

Grain-size measurements were corroborated by SEM micrographs obtained for $Bi_{0.85}Pr_{0.105}V_{0.045}O_{1.545}$ *nat*-powder (Fig. 4a) and *at*-powder (Fig. 4b). Two groups of particles sizes can be distinguished in Fig. 4a and a homogeneous powder is observed in Fig. 4b.

TABLE 1
Powder X-Ray Diffraction Data for $Bi_{0.85}Pr_{0.105}V_{0.045}O_{1.545}$

h	k	l	$d_{obs.}$	$d_{calc.}$	I/I_0 (%)
1	1	1	3.2069	3.2056	100
2	0	0	2.7778	2.7768	42
2	2	0	1.9637	1.9632	37
3	1	1	1.6747	1.6744	34
2	2	2	1.6034	1.6031	11
4	0	0	1.3882	1.3880	6
3	3	1	1.2742	1.2740	6
4	2	0	1.2418	1.2416	6
4	2	2	1.1338	1.1337	4
3	3	3	1.0689	1.0688	4
5	3	1	0.9387	0.9386	4
6	0	0	0.9255	0.9255	3

Note. Refined parameter $a = 5.5532(3)$ Å.

Nat-powder and *at* powder exhibit similar X-ray diagrams but it has been observed that the attrition treatment induces a reflection line widening linked to the particle size decreasing (inferior to 1 μm).

3.2. Sintering Behavior and Ceramic Microstructure

Curves showing diminution of pellet thickness with heating for the pellets prepared from *nat*-powder (*nat*-pellet) and

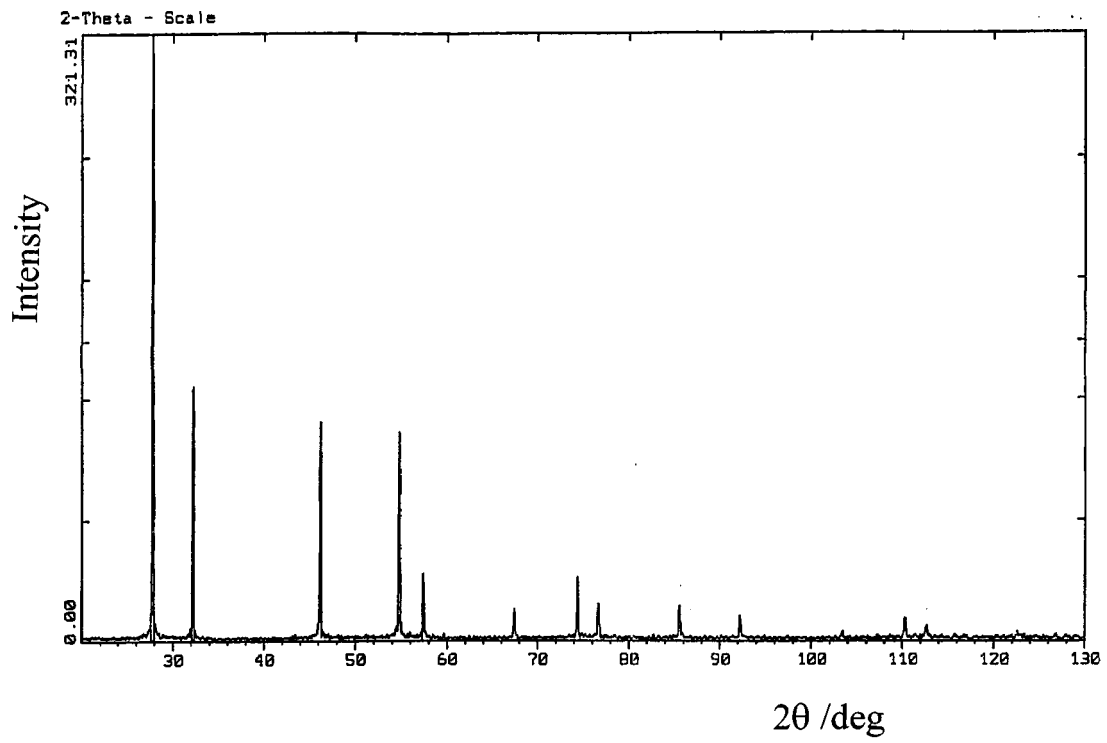

FIG. 1. X-ray diffraction pattern for $Bi_{0.85}Pr_{0.105}V_{0.045}O_{1.545}$ *nat*-powder.

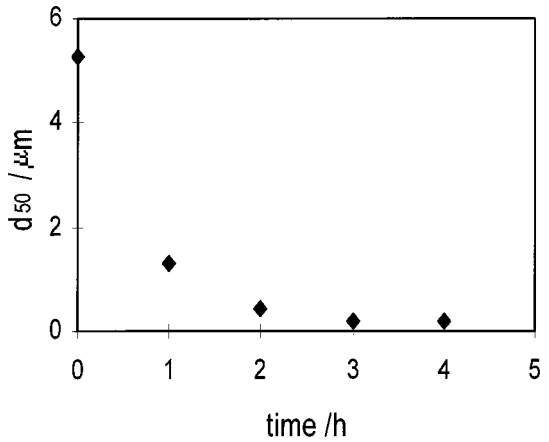

FIG. 2. Evolution of particle mean size (d_{50}) versus attrition time.

at-powder (*at*-pellet) are given in Fig. 5. For each pellet, the green relative density is nearly 61 $\pm$ 1%.

The differences in densification behavior of the *nat*-pellet and the *at*-pellet are clearly demonstrated. Shrinkage begins

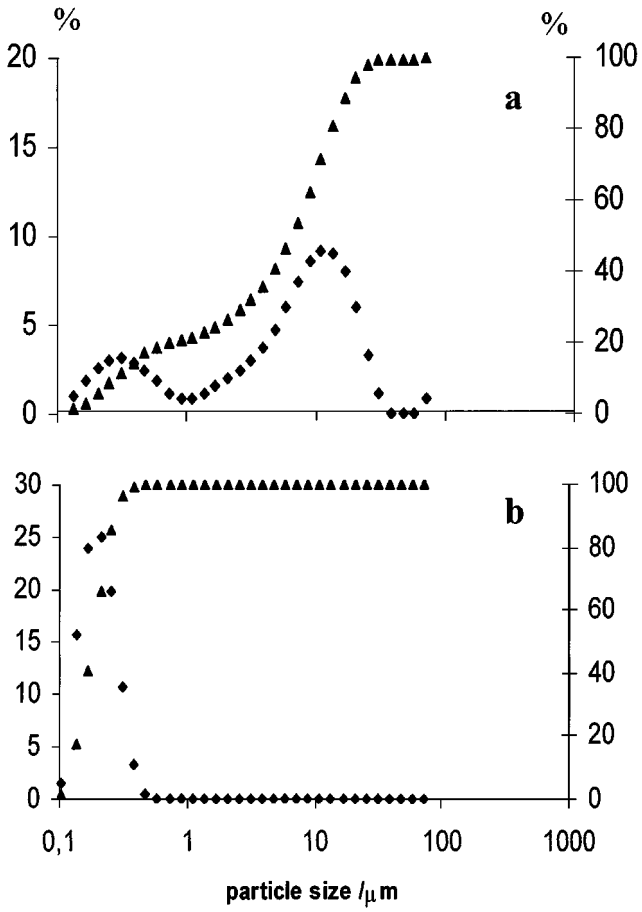

FIG. 3. Statistical distributions (vol%) versus the particle size (◆) and cumulative percentages undersize curve (▲) for *nat*-powder (a) and *at* powder (b).

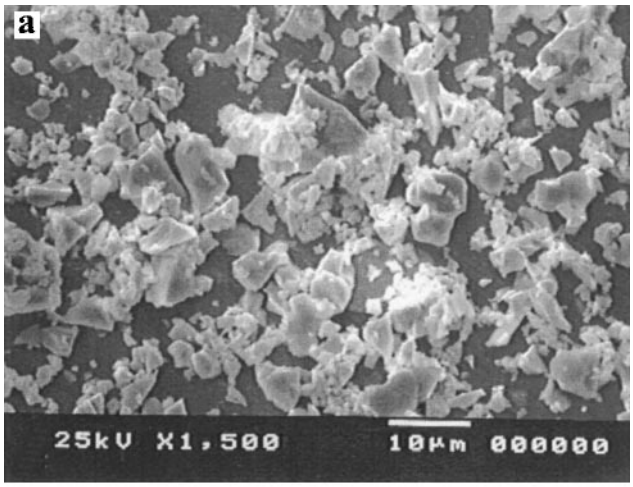

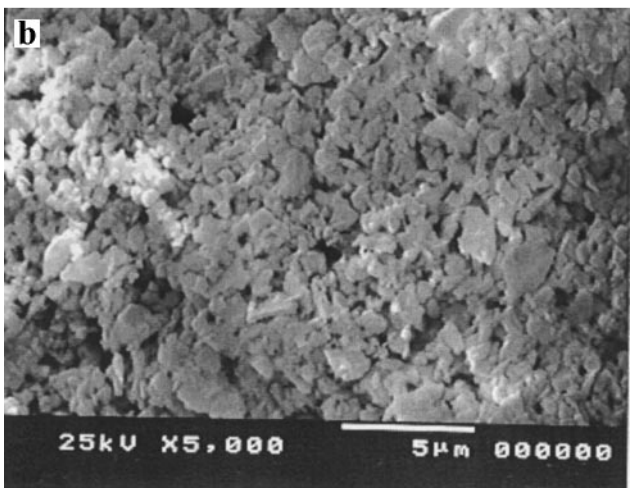

FIG. 4. SEM micrographs for *nat*-powder (a) and *at*-powder (b).

at about 550°C for the *at*-pellet and at 720°C for the *nat*-pellet. The sintering of the *nat*-pellet progresses to a shrinkage of 8% at 900°C, the limit of investigation; for the *at*-pellet, sintering is complete at 900°C with maximum shrinkage (slightly larger than 19%).

This difference in sintering behavior is directly linked to the particle size of the raw powder. Minimization of the particle size of the material (from 8.4 to 0.4 µm), by attrition treatment of the *nat* $Bi_{0.85}Pr_{0.105}V_{0.045}O_{1.545}$ powder, leads to more reactive particles and thus maximum density for *at*-pellets sintered at 900°C. Indeed, after 1 h at this temperature, the *nat*-pellets and *at*-pellets had average relative densities of 84 $\pm$ 1 and 98 $\pm$ 1%, respectively.

Diminishing the uniaxial pressure, to a minimum value, during the pellet preparation process allowed for a decrease of the green relative density of *at*-pellets from 61 to 43%. Thus, the dilatometric investigation revealed a behavior analogous to that of the previous *at*-pellet similarly heated, but length contraction was increased from 19 to 32%. The

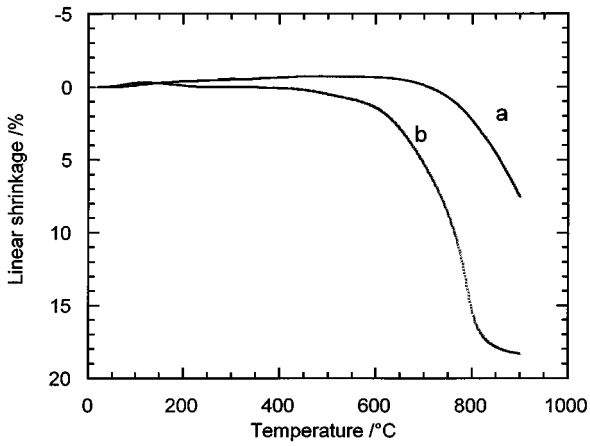

FIG. 5. Dilatometry curves of green pellets of *nat*-powder (a) and *at*-powder (b).

final relative density after heating at 900°C for 1 h was also nearly 98%.

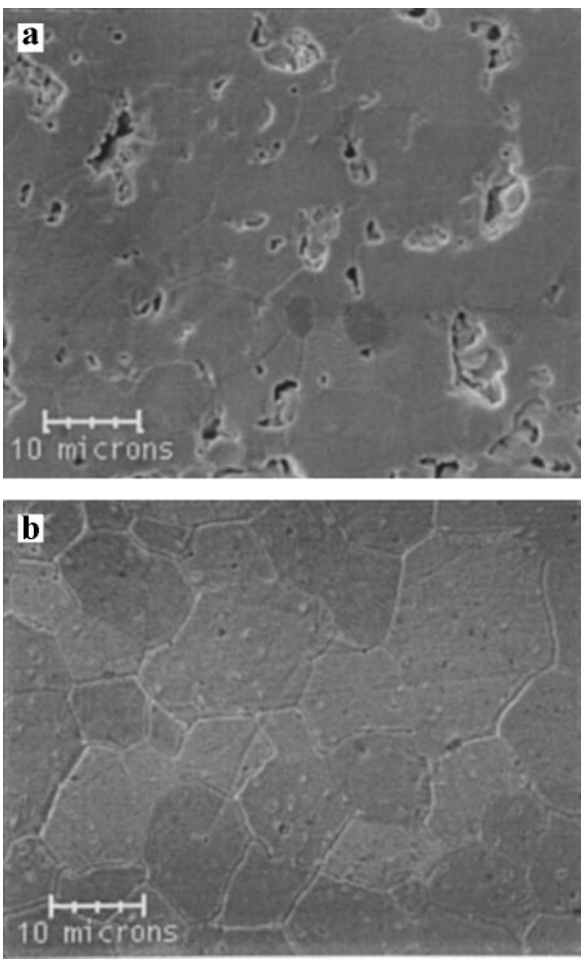

FIG. 6. SEM micrographs for *nat*-pellet (a) and *at*-pellet (b) sintered at 900°C (polished and thermally etched surface).

SEM micrographs, for the *nat*-pellet and the *at*-pellet sintered at 900°C, are presented in Figs. 6a and 6b. The *nat*-pellet microstructure has significant intergranular porosity (with estimated pore size between 2 and 5 μm), whereas the *at*-pellet is fully dense in agreement with the relative density values. Because of the high heterogeneity of grain shapes and the presence of pores, it was not possible to quantify the grain size of the *nat*-pellet. The estimated grain size of the *at*-pellet is between 10 and 20 μm. The observed microstructural differences for the two samples are a consequence of the different particle shapes and distribution of the starting powders.

3.3. Electrical Properties

Isothermal (200°C) impedance spectroscopy was performed on both types of pellets (Fig. 7), in order to identify the different parts of the spectra. The two impedance diagrams were normalized to a geometrical factor equal to 1. In each case, the diagram exhibits two well-defined semicircles: A high-frequency (HF) semicircle between 10^7 and 10^3 Hz and a low-frequency (LF) semicircle at frequency of less than 10^2 Hz.

The low relaxation frequency of about 10^{-1} Hz (at 200°C) of the LF semicircle suggests that this semicircle corresponds to the electrode response. To confirm this, a further impedance measurement was carried out, substituting a silver electrode for the gold electrode of the *at*-pellet. It is well known that variation of electrode materials modifies only the electrolyte/electrode interface reaction response on the impedance diagram (15). In fact, only the LF semicircle was modified by changing the electrode material with no effect on the HF semicircle.

If the electrode response is subtracted, both *nat*-pellet (84% compactness) and *at*-pellet (98% compactness) present only one semicircle. Impedance diagrams of polycrystalline

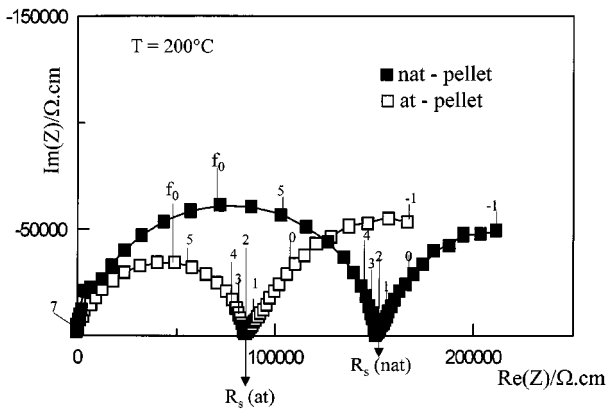

FIG. 7. Impedance diagrams (200°C) of *nat*-pellet (■) and *at*-pellet (□) sintered at 900°C. R_S indicates the sample resistance. The numbers −1, 0, 1, ... 7 indicate the logarithms of the measuring frequencies.

conductors usually show two semicircles related to the bulk and grain boundary responses (15–18). It is surprising that the impedance diagram for the $Bi_{0.85}Pr_{0.105}V_{0.045}O_{1.545}$ ceramic oxide has only one semicircle.

The observed semicircle was fitted using the Z view program. Table 2 shows the fitted parameters for the HF semicircles of the *at*- and *nat*-pellets. The differences in semicircle diameter (total sample resistivity, R_s) can be attributed to the presence of pores (16%) in the nat-pellet, consistent with the expectation that electrical resistivity of a material increases with increasing porosity (15,19).

Both samples have, approximately, the same value for the relaxation frequency. This is an indication that the HF semicircle characterizes the same electrical transport properties. HF semicircles for the *nat*- and the *at*-pellets have the same depression angle values, despite the porosity difference.

Capacitance values obtained for the HF fitted semicircles have the same order of magnitude (10^{-11}), within the expected range of bulk response.

The influence of porosity and grain size on the impedance response of the $Bi_{0.85}Pr_{0.105}V_{0.045}O_{1.545}$ materials are under investigation to confirm the existence of only one high-frequency contribution to the impedance spectra. Those results will be presented in a future paper (20).

Figure 8 presents the Arrhenius plots for both pellets. Conductivity varies similarly with pellet density. Each plot exhibits, as a first approximation, a linear domain in the low temperature range ($1000/T \geq 1.5$), whereas a curved region is observed at higher temperature. The experimental limit does not allow delineation of a linear domain in the high temperature range.

The significant change in slope must represent a cation and/or anion ordering within the structure in the low temperature range, which disappears when the temperature increases beyond the range 400–500°C. This structural modification, which has been proposed by different authors for the bismuth-based fluorite-type oxides, is corroborated for $Bi_{0.85}Pr_{0.105}V_{0.045}O_{1.545}$ by the observation of two domains of cell parameter during thermal treatment (12). Such transformation, during a slow annealing at 500°C, has been identified from progressive conductivity evolution for Bi–Er similar oxides (21). The slow structural modification, below 500°C, is likely responsible for the diversion from linearity.

TABLE 2
Parameters for Normalized HF Semicircles of *nat*-Pellet and *at*-Pellet Impedance Spectra

Parameter	Sample	
	nat-pellet	*at*-pellet
Resistivity ρ = diameter (Ω. cm)	150,400	84,800
Depression angle β (°)	11	11
Relaxation frequency f^0 (Hz)	1.7×10^5	1.6×10^5
Capacity $C_{(\rho C \omega^0 = 1)}$ (F)	0.63×10^{-11}	1.1×10^{-11}

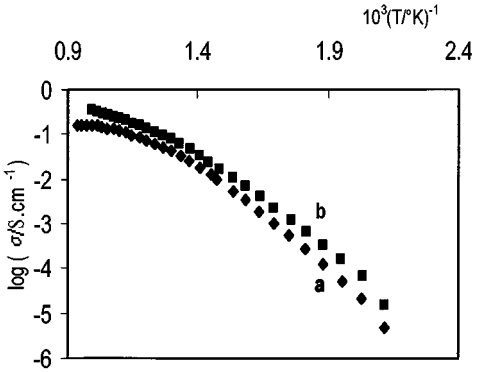

FIG. 8. Arrhenius plot of the electrical conductivity for *nat*-pellet (a) and *at*-pellet (b) sintered at 900°C.

For the same temperature range, activation energies are similar for both pellets, whereas the conductivity of the *at*-pellet is nearly twice that of the *nat*-pellet, in agreement with the difference of resistivity observed for the impedance diagrams recorded at 200°C (Fig. 7). These results considered altogether (Fig. 7 and Fig. 8) demonstrate that the electrical characterizations of a sample prepared from powder without particle size optimization must take into account the remaining porosity.

4. CONCLUSION

This investigation has demonstrated the relative ease of improvement of the quality of a sintered bismuth-based oxide material ($Bi_{0.85}Pr_{0.105}V_{0.045}O_{1.545}$), using a powder attrition treatment of the raw mixed oxide. The comparative study of a powder sample that received no attrition treatment (*nat*-powder) and one that underwent attrition treatment (*at*-powder) has revealed the following:

— *nat*-powder contains two families of grain size centered at 0.31 and 11 μm. Four hours of milling breaks up particles, inducing a decrease of the mean grain size to 0.4 μm.

— Pellets prepared from *nat*-powder or *at*-powder, respectively, can be distinguished by physical shrinkage which starts at 720 or 550°C; the final relative density which reaches 84 or 98% at 900°C; the microstructure of the material, heterogeneous and porous for the *nat*-pellet or homogeneous and dense for the *at*-pellet; the electrical resistance of the *nat*-pellet, which is twice that of the *at*-pellet when the corresponding capacities a 1/2 ratio.

These observations seem to indicate, contrary to what is usually observed for sintered oxygen ionic conductors, that

the material, grain boundary, and pore contributions to impedance are characterized inside only one semicircle.

REFERENCES

1. T. Takahashi, H. Iwahara, and Y. Nagai, *J. Appl. Electrochem.* **2,** 97 (1972).
2. H. A. Harwig, *Z. Anorg. Allg. Chem.* **444,** 151 (1978).
3. P. Conflant, J. C. Boivin, and D. Thomas, *J. Solid State Chem.* **18,** 133 (1976).
4. P. Conflant, Thesis, Lille University, 1985.
5. M. Omari, Thesis, Lille University, 1989.
6. P. Conflant, C. Follet-Houttemane, and M. Drache, *J. Mater. Chem.* **1,** 649 (1991).
7. A. El Harrak, P. Conflant, M. Drache, and J. C. Boivin, *J. Chim. Phys.* **88,** 2281 (1991).
8. M. Omari, M. Drache, P. Conflant, and J. C. Boivin, *Solid State Ionics* **40–41,** 929 (1990).
9. N. Portefaix, P. Conflant, J. C. Boivin, J. P. Wignacourt, and M. Drache, *J. Solid State Chem.* **134,** 219 (1997).
10. R. D. Shannon and C. T. Prewitt, *Acta Crystallogr. Sect. B* **26,** 10467 (1970).
11. R. D. Shannon, *Acta Crystallogr. Sect. A* **32,** 751 (1976).
12. M. Benkaddour, unpublished results.
13. S. P. Simner, D. Suarez-Sandoval, J. D. Mackenzie, and B. Dunn, *J. Am. Ceram. Soc.* **80,** 2563 (1997).
14. M. C. Steil, J. Fouletier, M. Kleitz, and P. Labrure, *J. Eur. Ceram. Soc.* **19,** 815 (1999).
15. M. C. Steil, F. Thévenot, and M. Kleitz, *J. Electrochem. Soc.* **144,** 390 (1997).
16. M. Kleitz, L. Dessemond, and M. C. Steil, *Solid State Ionics* **75,** 107 (1995).
17. S. P. J. Badwal, *Solid State Ionics* **76,** 67 (1995).
18. K. Huang, M. Feng, J. B. Goodenough, and M. Schmerling, *J. Electrochem. Soc.* **143,** 3630 (1996).
19. R. Landauer, *in* "Proceedings of AIP Conference" (J. C. Garland and D. B. Tanner, Eds.), Vol. 40, pp. 2–45. American Institute of Physics, New York, 1978.
20. M. Benkaddour, M. C. Steil, P. Conflant, and M. Drache, *Solid State Ionics* (2000), submitted.
21. N. Jiang and E. D. Wachsman, *J. Am. Ceram. Soc.* **82,** 3057 (1999).